<div align="center">

Supplementary Information for

Equation of state for water and its line of density maxima down to -120 MPa

</div>

Gaël Pallares[1], Miguel Angel Gonzalez[2], Jose Luis F. Abascal[2], Chantal Valeriani[2] and Frédéric Caupin[1]

[1] *Institut Lumière Matière, UMR5306 Université Claude Bernard Lyon 1-CNRS,*
Université de Lyon and Institut Universitaire de France, 69622 Villeurbanne cedex, France and

[2] *Departamento de Quimica Fisica I, Facultad de Ciencias Quimicas, Universidad Complutense, 28040 Madrid, Spain*

<div align="center">

Materials and methods

</div>

All details concerning the samples and the sound velocity measurements can be found in Ref. 1. In brief, we have studied two inclusions of pure water in a quartz crystal. Sample 1 is synthetic, and Sample 2 is natural (from the French Alps). If a bubble is present in a sample, it shrinks upon heating and disappears at the homogeneization temperature T_{h}. Upon further cooling, the sample follows a quasi-isochore and a negative pressure develops[2–5]. The samples were chosen for their low cavitation probability during cooling, which allow to reach the doubly metastable region where liquid water is at the same time metastable with respect to vapor and ice. The sound velocity was measured with Brillouin light scattering in backscattering geometry, with a 532 nm laser. The typical uncertainty on sound velocity is $6\,\mathrm{m\,s^{-1}}$[1]. The experimental values are listed in Table S1. The homogeneization temperatures of the samples determined by Brillouin light scattering[6] are $T_{\mathrm{h},1} = 131.8 \pm 0.6°\mathrm{C}$ and $T_{\mathrm{h},2} = 108.8 \pm 0.7°\mathrm{C}$, respectively, which corresponds to densities at homogenization of $\rho_1(T_{\mathrm{h},1}) = 933.3 \pm 0.5\,\mathrm{kg\,m^{-3}}$ and $\rho_2(T_{\mathrm{h},2}) = 951.9 \pm 0.6\,\mathrm{kg\,m^{-3}}$, respectively.

We have performed Molecular Dynamics (MD) simulations of a system of 500 water molecules at constant temperature and pressure (NPT ensemble) interacting by means of the TIP4P/2005 potential[7] with periodic boundary conditions. TIP4P/2005 represents water as a rigid and non-polarizable molecule. It consists of a Lennard-Jones site centred at the oxygen atom and a Coulomb interaction given by two partial charges placed at the hydrogen atom and a negative one placed at a point M along the bisector of the HOH angle.

The parametrization of TIP4P/2005 has been based on a fit of the temperature of maximum density and a variety of properties of the liquid and the ice polymorphs. TIP4P/2005 has been used to calculate a broad range of thermodynamic properties of the liquid and solid phases, such as the phase diagram involving condensed phases[8–10], properties at melting and vaporization[11,12], dielectric constants[13], pair distribution function, and self-diffusion coefficient. These properties cover a temperature range from 123 to 573 K and pressures up to 4000 MPa[14]. We have performed MD simulations with the GROMACS 4.5 package [15,16] using the particle mesh Ewald method [17] to calculate the long-range electrostatics forces and the SHAKE algorithm[18] to constrain the intramolecular degrees of freedom. We set

TABLE S1: Sound velocity in $\mathrm{m\,s^{-1}}$ measured for samples 1 and 2. Uncertainty is $\pm 6\,\mathrm{m\,s^{-1}}$ unless otherwise indicated.

Temperature (°C)	Sample 1 $\rho_1 = 933.3\,\mathrm{kg\,m^{-3}}$	Sample 2 $\rho_2 = 951.9\,\mathrm{kg\,m^{-3}}$	Temperature (°C)	Sample 1 $\rho_1 = 933.3\,\mathrm{kg\,m^{-3}}$	Sample 2 $\rho_2 = 951.9\,\mathrm{kg\,m^{-3}}$
-15	1338.4		5	1321.4	
-12	1332.3	1360.7 ± 6.8	10	1329.1	1379.4
-12		1340.5 ± 6.3	22.6	1335.9	
-10		1349.5 ± 7.8	25	1336.6	1391.6
-10		1325.2	30	1349.2	1408.0
-9	1318.4		33		1400.3
-6	1313.5		40	1357.8	1421.5
-3	1312.4		50	1369.1	1437.0
0	1305.0	1357.9	60	1387.1	1464.2
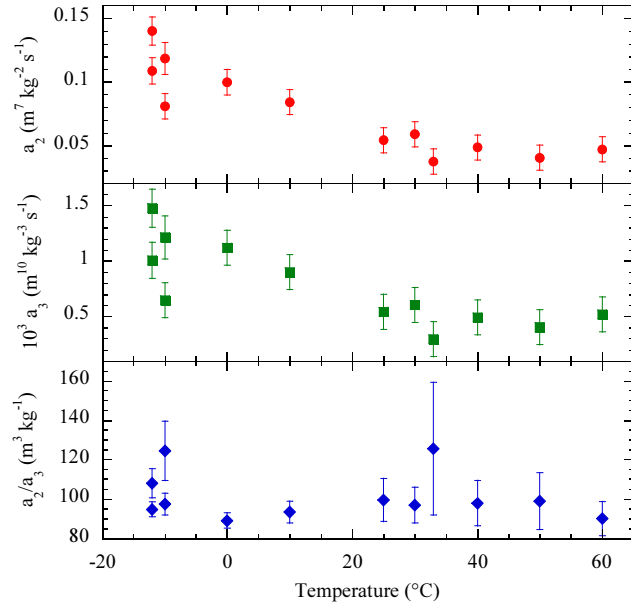
FIG. S1: Parameters a_2 (upper panel), a_3 (mid panel), and their ratio a_2/a_3 (lower panel), computed from Eq. S.1 at each temperature of the sample 2 data. The error bars are calculated from the uncertainty on the sound velocity.

the time step to 1 fs and make use of the Nosé-Hoover thermostat[19,20] and the Parrinello-Rahman barostat,[21] with coupling constants set to 2 ps. The Lennard-Jones interactions are switched from 0.85 nm and truncated at 0.95 nm. The contributions to the energy and pressure beyond this distance are approximated assuming that the molecules are uniformly distributed.

Choice of the interpolating function

The first step of our analysis is to choose a simple analytic function $c_{\mathrm{int}}(T, \rho)$ to interpolate the sound velocity data between the stable region and the largest negative pressure achieved. For simplicity we assume a polynomial density dependence of c_{int} at each temperature. To reproduce the experimental density behavior for $c(T, \rho)$ (non-monotonic at low temperature), a third order polynomial is needed. The interpolating function writes:

$$c_{\mathrm{int}}(T, \rho) = c(T, \rho_0) + \left(\frac{\partial c}{\partial \rho}\right)_T (T, \rho_0) \left(\rho - \rho_0\right) + a_2(T) \left(\rho - \rho_0\right)^2 + a_3(T) \left(\rho - \rho_0\right)^3 , \qquad (\text{S.1})$$

where a_2 and a_3 are functions of the temperature to be determined. We start with a reference isochore at $\rho_0 = 1000 \, \mathrm{kg\,m^{-3}}$ on which water properties are known accurately through a multi-parameter equation of state, the IAPWS EoS[22]. We impose the known values of $c(T, \rho_0)$ and $(\partial c/\partial \rho)_T(T, \rho_0)$. At a given temperature T, there is a unique pair of values (a_2, a_3) for which Eq. S.1 reproduces the values of $c(T, \rho_1)$ and $c(T, \rho_2)$ taken from the two samples. We first compute this solution for (a_2, a_3) at each temperature for which data is available for sample 2, using the corresponding data for sample 1 (or a linear interpolation between the neighboring data points for -10 and $-30°$C). The result is shown on Fig. S1, with the error bars deduced from the experimental uncertainty on the sound velocity. Parameters a_2 and a_3 exhibit a smooth temperature variation, and their ratio (Fig. S1, lower panel) is remarkably constant. These observations suggest to use simple interpolating functions for the whole set of $c(T, \rho)$ data. We have investigated 10 possible choices for $a_2(T)$ and $a_3(T)$, listed in Table S2. For 5 of them, a_2 and a_3 have the same functional form but independent parameters. For the other 5, the ratio a_2/a_3 is kept constant, which means that the inflection point in $c_{\mathrm{int}}(T, \rho)$ at each T occurs for the same value of ρ. The fits and their residuals are displayed on Figs. S2 and S3, respectively. Given the number of fitting parameters and the fit quality in terms of the reduced χ^2 (Table S2), we chose to use in the following the interpolations 8 and 10. This will allow to check the sensitivity of the results on the interpolation function.
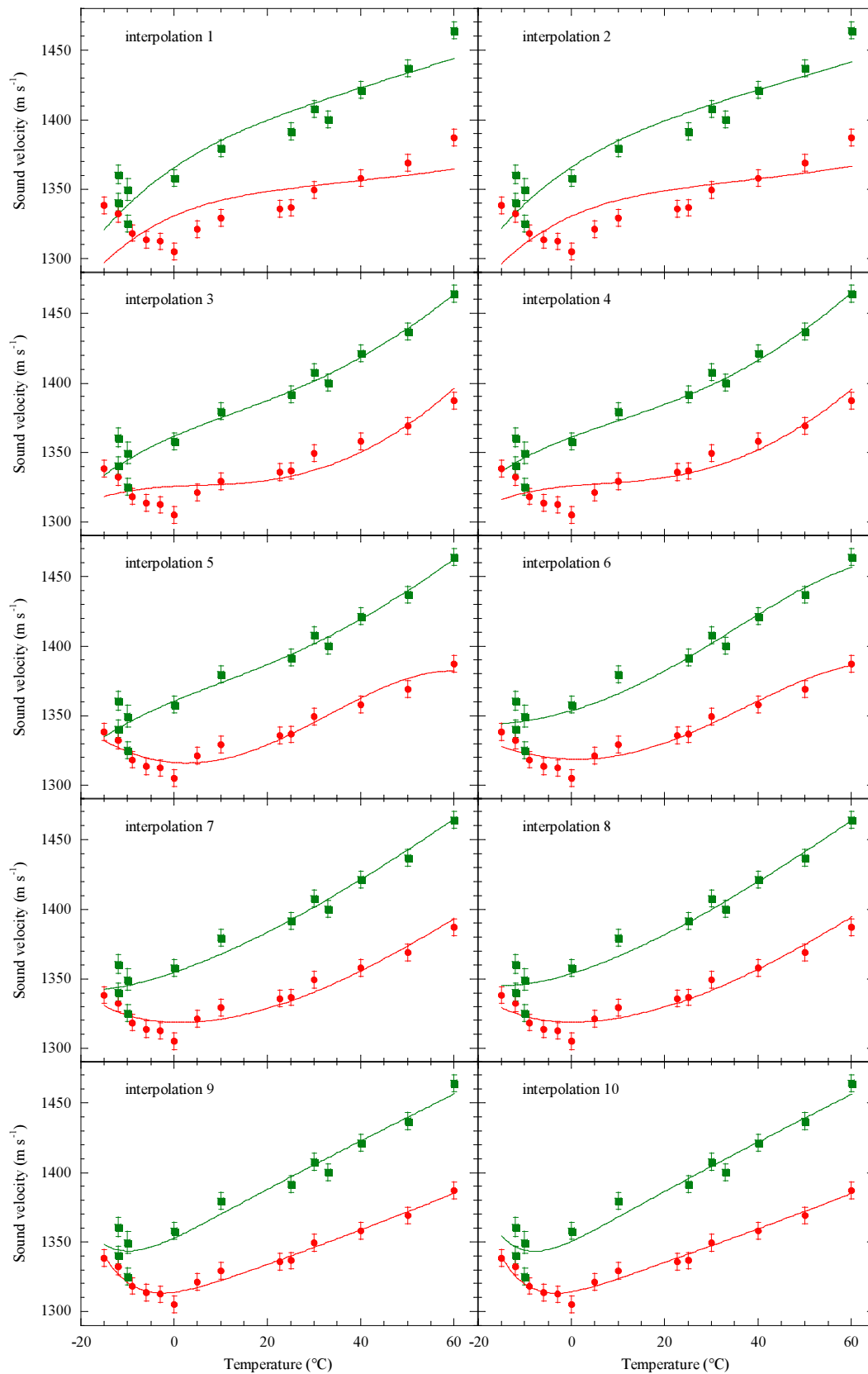
FIG. S2: Best fit of the whole set of experimental data given in Table S1 obtained with the interpolations listed in Table S2. The right column corresponds to interpolations for which the ratio a_2/a_3 is kept constant.
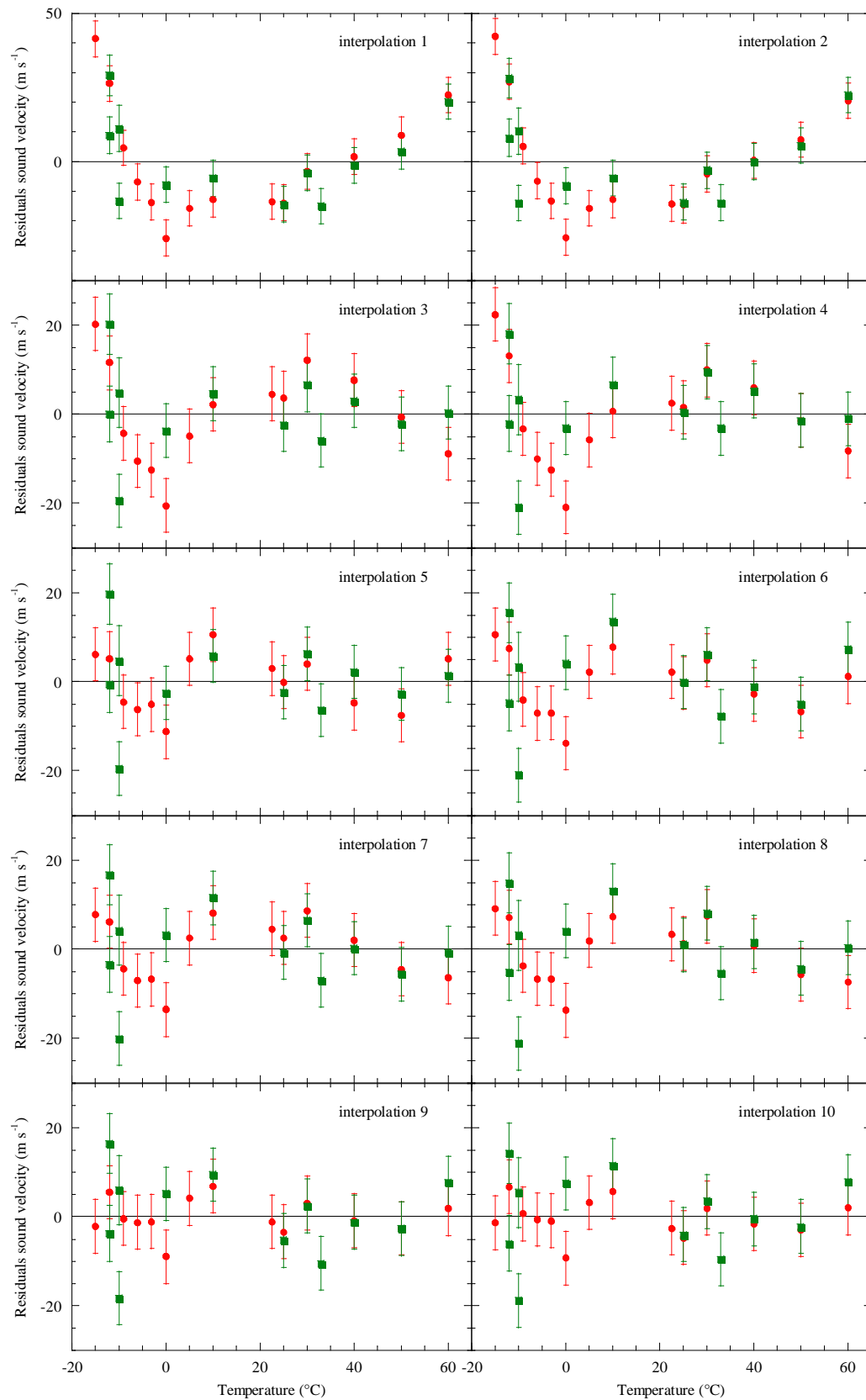
FIG. S3: Residuals of the fits of the whole set of experimental data given in Table S1 obtained with the interpolations listed in Table S2. Note the different vertical scale in the first row. The right column corresponds to interpolations for which the ratio a_2/a_3 is kept constant.

TABLE S2: Functions used for a_2 and a_3 in Eq. S.1 in order to fit the experimental data set of Table S1. The corresponding number of fitting parameters p and reduced χ^2 are also given.

Interpolation n°	$a_2(T)$	$a_3(T)$	p	χ^2
1	$m_{20} + m_{21}T$	$m_{30} + m_{31}T$	4	8.39
2	$m_{20} + m_{21}T$	$a_2(T)/K$	3	8.06
3	$m_{20} + m_{21}T + m_{22}T^2$	$m_{30} + m_{31}T + m_{32}T^2$	6	3.40
4	$m_{20} + m_{21}T + m_{22}T^2$	$a_2(T)/K$	4	3.19
5	$m_{20} + m_{21}T + m_{22}T^2 + m_{23}T^3$	$m_{30} + m_{31}T + m_{32}T^2 + m_{33}T^3$	8	2.14
6	$m_{20} + m_{21}T + m_{22}T^2 + m_{23}T^3$	$a_2(T)/K$	5	2.20
7	$m_{20} + m_{2e}e^{-T/\theta}$	$m_{30} + m_{3e}e^{-T/\theta}$	6	2.15
8	$m_{20} + m_{2e}e^{-T/\theta}$	$a_2(T)/K$	4	2.03
9	$m_{20} + m_{21}T + m_{2e}e^{-T/\theta}$	$m_{30} + m_{31}T + m_{3e}e^{-T/\theta}$	8	1.74
10	$m_{20} + m_{21}T + m_{2e}e^{-T/\theta}$	$a_2(T)/K$	5	1.54

Construction of an equation of state from sound velocity data along isochores

Our analysis is based on the fact that it is possible to build an equation of state from a series of sound velocity measurements over a given region of the phase diagram[23,24]. Usually, the sound velocity is measured as a function of temperature and pressure. The procedure then uses as a starting point the sound velocity c, the density ρ and the isobaric heat capacity C_P along a reference starting isobar at pressure P, from which thermodynamic relations are integrated to give the ρ and C_P over the temperature and pressure ranges in which the sound velocity data is available. In our case, the natural variable is density rather than pressure. Consequently, the starting point is c, P, and C_V along a reference starting isochore ($\rho_{\text{ref}} = 1000 \, \text{kg m}^{-3}$). The set of thermodynamic relations to be integrated also differs; to our knowledge, the procedure adapted to the density variable has not been reported before, so we give the details here. The relevant relations are:

$$c^2 = \left(\frac{\partial P}{\partial \rho}\right)_T + \frac{T}{\rho^2 C_V}\left(\frac{\partial P}{\partial T}\right)_\rho , \tag{S.2}$$

$$\left(\frac{\partial C_V}{\partial \rho}\right)_T = -\frac{T}{\rho^2}\left(\frac{\partial^2 P}{\partial T^2}\right)_\rho . \tag{S.3}$$

To integrate them, we use a grid of $T - \rho$ values (with steps δT and $\delta \rho$) and follow a predictor-corrector scheme[24]:

1. from an isochore at density ρ along which c, C_V, $(\partial P/\partial T)_\rho$ and $(\partial^2 P/\partial T^2)_\rho$ are known, Eqs. S.2 and S.3 give $(\partial P/\partial \rho)_T(\rho, T)$ and $(\partial C_V/\partial \rho)_T(\rho, T)$.

2. first estimates for P and C_V at the next density $\rho' = \rho + \delta\rho$ on the grid are obtained through:

$$P(\rho', T) = P(\rho, T) + \left(\frac{\partial P}{\partial \rho}\right)_T (\rho, T)\delta\rho , \tag{S.4}$$

$$C_V(\rho', T) = C_V(\rho, T) + \left(\frac{\partial C_V}{\partial \rho}\right)_T (\rho, T)\delta\rho . \tag{S.5}$$

3. The list of $P(\rho', T)$ values is fitted with a 8th order polynomial, to compute $(\partial P/\partial T)_\rho$ and $(\partial^2 P/\partial T^2)_\rho$.

4. From the values c, C_V, $(\partial P/\partial T)_\rho$ and $(\partial^2 P/\partial T^2)_\rho$ along the isochore at density ρ', $(\partial P/\partial \rho)_T(\rho', T)$ and $(\partial C_V/\partial \rho)_T(\rho', T)$ are calculated with Eqs. S.2 and S.3.

5. A refined value for P and C_V at density ρ' is then obtained:

$$P(\rho', T) = P(\rho, T) + \frac{1}{2}\left[\left(\frac{\partial P}{\partial \rho}\right)_T (\rho, T) + \left(\frac{\partial P}{\partial \rho}\right)_T (\rho', T)\right]\delta\rho , \tag{S.6}$$

$$C_V(\rho', T) = C_V(\rho, T) + \frac{1}{2}\left[\left(\frac{\partial C_V}{\partial \rho}\right)_T (\rho, T) + \left(\frac{\partial C_V}{\partial \rho}\right)_T (\rho', T)\right]\delta\rho . \tag{S.7}$$

6. A new fit of $P(\rho', T)$ values with a 8th order polynomial is performed, to compute $(\partial P/\partial T)_\rho$ and $(\partial^2 P/\partial T^2)_\rho$.
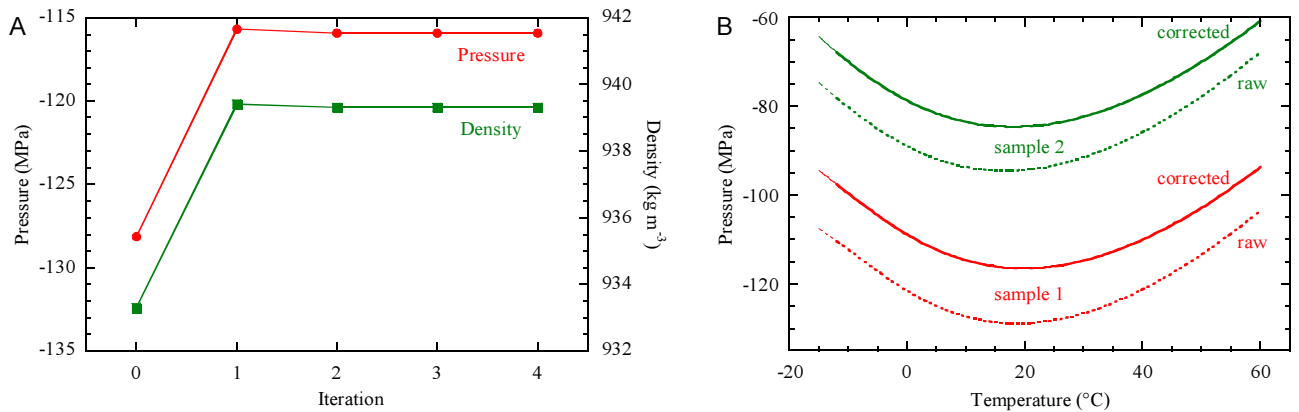
FIG. S4: Convergence of the iterative procedure accounting for the quartz compliance, using interpolation 10. A. Pressure and density for sample 1 at 20°C for successive iterations. B. Pressure as a function of temperature for samples 1 and 2 from the initial data assuming constant densities (dotted curves), and after 4 iterations (solid curves). The thinner sections below −12°C show the parts based on data extrapolated from sample 2.

The procedure is then repeated starting from ρ' to compute properties on the next isochore at $\rho' + \delta\rho$. We have used $\delta T = 0.5\,\mathrm{K}$ and $\delta\rho = 0.1\,\mathrm{kg\,m^{-3}}$. We checked that using $\delta T = 1\,\mathrm{K}$ or $\delta\rho = 0.025\,\mathrm{kg\,m^{-3}}$ did not affect the results.

Usual thermodynamic relations have been also used to compute the isothermal compressibility κ_T and the isobaric heat capacity C_P:

$$\kappa_T = \frac{1}{\rho}\left(\frac{\partial\rho}{\partial P}\right)_T , \tag{S.8}$$

$$C_P = C_V\left[1 + \frac{T}{\rho^2 C_V}\left(\frac{\partial P}{\partial T}\right)_\rho^2\left(\frac{\partial\rho}{\partial P}\right)_T\right] . \tag{S.9}$$

TABLE S3: Sound velocity, density and pressure for the experimental data points after 4 iterations, using interpolation 8.

	Sample 1			Sample 2		
Temperature	Sound velocity	Density	Pressure	Sound velocity	Density	Pressure
(°C)	($\mathrm{m\,s^{-1}}$)	($\mathrm{kg\,m^{-3}}$)	(MPa)	($\mathrm{m\,s^{-1}}$)	($\mathrm{kg\,m^{-3}}$)	(MPa)
-15	1335.8	940.9	-92.9			
-12	1329.8	940.8	-97.0	1358.6	958.0	-67.7
-12				1338.4	958.0	-67.7
-10				1347.4	957.9	-70.0
-10				1323.2	957.9	-70.0
-9	1316.0	940.6	-100.8			
-6	1311.1	940.5	-104.0			
-3	1310.0	940.4	-106.8			
0	1302.7	940.3	-109.2	1356.0	957.5	-78.9
5	1319.1	940.1	-112.4			
10	1326.9	939.9	-114.5	1377.6	957.1	-83.5
22.6	1333.9	939.3	-116.0			
25	1334.6	939.2	-115.6	1390.0	956.5	-83.6
30	1347.2	939.0	-114.4	1406.4	956.3	-82.1
33				1398.8	956.1	-81.0
40	1356.0	938.6	-109.9	1420.1	955.9	-77.2
50	1367.4	938.2	-103.3	1435.7	955.4	-70.2
60	1385.5	937.8	-94.7	1463.0	955.0	-61.3

Correction due to quartz compliance

Because of the finite thermal expansion and compressibility of quartz, the inclusion shrinks during cooling, and as the negative pressure builds up in the liquid. For a given sample, the liquid density will therefore vary with temperature: $\rho(T) \geq \rho(T_h)$ for $T \leq T_h$. In the temperature and pressure range investigated, the volume expansion coefficient of quartz is constant: $\alpha_V = 4.43 \, 10^{-6} \, \mathrm{K}^{-1}$ [25]. To account for the elasticity of quartz, for simplicity, we treat the inclusion as a spherical cavity inside an infinite, isotropic medium with bulk modulus B and Poisson ration ν. We use parabolic fits to the data between 19 and 196°C from Ref. 26. In this range, B and ν decrease from 38.17 to 35.70 GPa, and from 0.078 to 0.060, respectively. A short extrapolation to -15°C is needed; it is fully justified by another study at low temperature [27]. The density of the liquid at temperature T when it exerts a pressure $P < 0$ on the quartz walls writes [28]:

$$\rho(T) = \rho(T_h) \left(1 + \alpha_V(T - T_h) + \frac{1+\nu}{1-2\nu} \frac{P}{2B} \right)^{-1} . \tag{S.10}$$

To include these effects in our analysis, we apply an iterative procedure. First, the EoS is calculated assuming that the fluid inclusions follow a perfect isochore at $\rho_1(T_{h,1})$ and $\rho_2(T_{h,2})$. From this first step we get an estimate of the pressure in the fluid inclusion as a function of temperature, which is fed into Eq S.10 to calculate the actual densities $\rho_1(T)$ and $\rho_2(T)$. For completeness we also recalculate the sound velocity of our primary data. Indeed, they are deduced from the measured Brillouin shift using the refractive index of water $n(\rho, T)$ that depends on density and temperature, so that the density change results in a factor $n[\rho_i(T_{h,i}), T]/n[\rho_i(T), T]$ (i=1,2). We note that this last correction is around $2 \, \mathrm{m \, s^{-1}}$ (compare Table S1 to Tables S3 and S4), below our uncertainty on the sound velocity. The new data for density and sound velocity is then used as described in the previous section, and the procedure is repeated until convergence is achieved. This takes only 4 iterations, as shown in Fig. S4 A. Thermal and elastic effects have typically the same contribution. The final data sets after 4 iterations is given in Tables S3 and S4 for interpolations 8 and 10, respectively. Fig. S4 B compares the actual pressure in the samples to the pressure which would correspond to a true isochoric path. In the $-15 - 60$°C range, the new pressure is actually close to the pressure along a shifted isochore, the density in sample 1 and 2 varying in the range $937.85 - 940.9$ and $955.05 - 958.15 \, \mathrm{kg \, m^{-3}}$, respectively. The maximum relative changes due to quartz compliance are 0.8% in density, and 14 % in pressure, consistent with a similar correction in Ref. 2.

TABLE S4: Sound velocity, density and pressure for the experimental data points after 4 iterations, using interpolation 10.

Temperature	Sample 1			Sample 2		
	Sound velocity	Density	Pressure	Sound velocity	Density	Pressure
(°C)	($\mathrm{m \, s^{-1}}$)	($\mathrm{kg \, m^{-3}}$)	(MPa)	($\mathrm{m \, s^{-1}}$)	($\mathrm{kg \, m^{-3}}$)	(MPa)
-15	1335.8	940.9	-94.6			
-12	1329.8	940.8	-97.6	1358.6	958.0	-67.8
-12				1338.4	958.0	-67.8
-10				1347.4	957.9	-70.0
-10				1323.2	957.9	-70.0
-9	1315.9	940.7	-100.6			
-6	1311.1	940.5	-103.7			
-3	1310.0	940.4	-106.4			
0	1302.7	940.3	-108.9	1356.0	957.5	-78.7
5	1319.1	940.1	-112.2			
10	1326.9	939.9	-114.6	1377.6	957.1	-83.5
22.6	1333.9	939.4	-116.3			
25	1334.6	939.3	-115.9	1390.0	956.5	-83.8
30	1347.2	939.1	-114.6	1406.4	956.3	-82.3
33				1398.8	956.2	-81.0
40	1356.0	938.7	-109.9	1420.1	955.9	-77.2
50	1367.4	938.3	-102.7	1435.7	955.5	-69.9
60	1385.5	937.8	-93.7	1463.0	955.0	-60.8
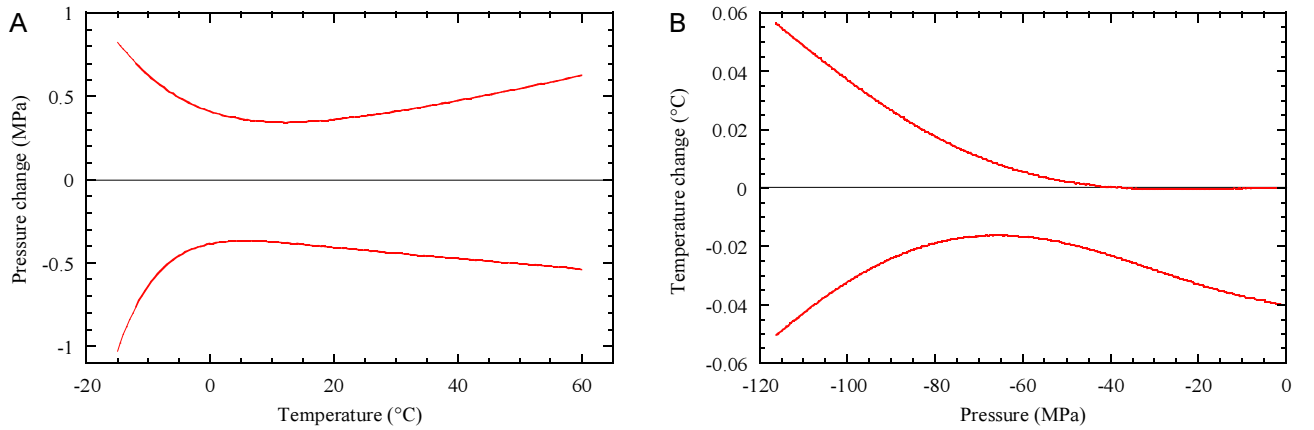
FIG. S5: Propagation of the uncertainty on sound velocity, using interpolation 10. A. Confidence interval for the pressure in sample 1. The thinner sections below $-12°$C show the parts based on data extrapolated from sample 2. B. Confidence interval for the temperature of the LDM.

Propagation of errors

To estimate the impact of the uncertainty on sound velocity on the results, we proceed as follows. We use interpolation 10. The first fit on the raw sound velocity data (Table S1) gives a mean prediction confidence interval on the fitted sound velocity values. We replace the experimental sound velocity values by the lower bound or upper bound of this interval. We then repeat the full procedure to generate the EoS for either choice by using the lower or upper bound as a new initial input data. The effect on the pressure is small. For instance, for the pressure in sample 1 (Figure S5A), the maximum change is only 1 MPa, to compare to a pressure in the 100 MPa range. The effect on the LDM is small too (Figure S5B), amounting to less than $0.06°$C at the largest negative pressure. The effect on derivatives such as the compressibility and heat capacity is more visible, as is shown on Figs. S6C and D. However, we will see in the next section that the results are more dependent on the choice of the interpolating function.

Results and sensitivity to the interpolation function

We have applied the procedure to generate the EoS, including the quartz compliance effects, with two of the interpolations listed in Table S2: 8 and 10. The best fit parameters are given in Table S5. The results are compared in Fig. S6. After correction for quartz compliance, the two fits are of comparable quality (Fig. S6A). The LDM is found to be a robust feature, with a difference between the two interpolations reaching at most $0.6°$C at the largest negative pressure (Fig. S6B). In contrast, although the absolute values of thermodynamic derivatives such as κ_T (Fig. S6C) and C_P (Fig. S6D) remain close, their variation is quite sensitive to the choice of interpolation: interpolation 10 finds maxima, whereas interpolation 8 finds a monotonic behavior. Therefore, although our best fit suggests the existence of extrema in the response functions of water around $-10°$C and -90 MPa, the present accuracy is not enough to ascertain them, and this issue will require further work.

TABLE S5: Best fit parameters for interpolation 8 and 10, before and after the iterative procedure accounting for quartz compliance.

Parameters	Units	Interpolation 8		Interpolation 10	
		initial data	after 4 iterations	initial data	after 4 iterations
m_{20}	$\mathrm{m^7\,kg^{-2}\,s^{-1}}$	0.0394	0.0323	0.0723	0.0683
m_{21}	$\mathrm{m^7\,kg^{-2}\,s^{-1}\,K^{-1}}$	—	—	-0.00061	-0.00067
m_{2e}	$\mathrm{m^7\,kg^{-2}\,s^{-1}}$	0.0461	0.0563	0.0105	0.0173
θ	K	21.0	19.7	8.6	9.6
K	$\mathrm{kg\,m^{-3}}$	99.7	87.6	99.4	87.4
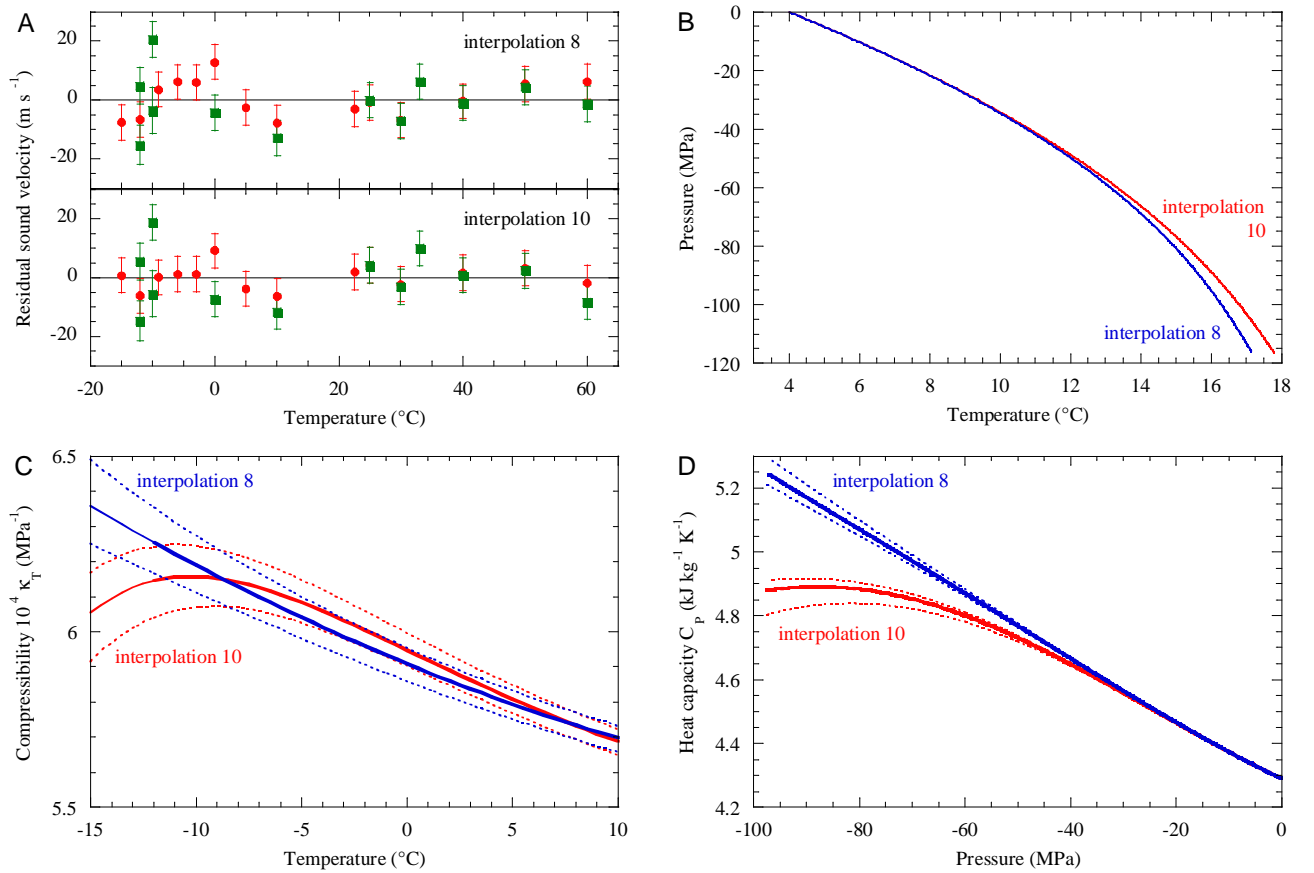
FIG. S6: Comparison of results obtained with interpolations 8 and 10. A. Residuals of the respective fits after the iteration procedure used to account for the quartz compliance. The reduced χ^2 are 1.88 and 1.56, respectively. B. Line of density maxima: the results from the two interpolations differ by $0.6°C$ at most. C. Isothermal compressibility along the $-90\,\text{MPa}$ isobar. Interpolation 10 finds a maximum at $-10°C$, while interpolation 8 finds a monotonic behavior. D. Isobaric heat capacity along the $-12°C$ isotherm. Interpolation 10 finds a maximum at $-88\,\text{MPa}$, while interpolation 8 finds a monotonic behavior.

Two state model for water

All details of the model can be found in the paper by Holten and Anisimov[29]. In brief, liquid water is treated as a mixture of two interconvertible states with a zero enthalpy of mixing, but an excess entropy of mixing proportional to the product of their molar fraction. Including background terms in the Gibbs free energy of the mixture, one can build an accurate representation of a set of 252 experimental data points from 140 to 310 K, and from 0.1 MPa to 400 MPa; they include data for density, isothermal compressibility, thermal expansion coefficient, isobaric heat capacity, and sound velocity. Moreover, this formulation includes a liquid-liquid critical point in the supercooled region. Two versions of the corresponding equation of state can be written: a mean-field version, and a crossover EoS including critical fluctuations. We use the mean-field version because it is much simpler to implement. The two versions give the same accurate description of experimental data, and differ only from each other close to the liquid-liquid critical point (whose location also changes between the two versions).

The parameters of the HA model were fitted to the available experimental data for water at positive pressure below $27°C$. The best fit parameters for the LLCP are: $-45°C$ and $0\,\text{MPa}$ for a mean field version[30], vs. $-46°C$ and $13\,\text{MPa}$ for a crossover equation incorporating critical fluctuations[29].

Calculation of the line of density maxima from numerical simulations of TIP4P/2005

In order to compute the LDM (or temperature of density maxima) in the $P-T$ plane, we simulate a 500 molecules system in the NPT ensemble to calculate the density. We checked that the difference in density between systems made of 500 and 4000 water molecules is comparable to the statistical uncertainty around $0.1\,\text{kg}\,\text{m}^{-3}$. Thus 500 molecules

Temperature	Pressure (MPa)							
(K)	100	40	0.1	-40	-75	-100	-125	-150
240	1044.9	1011.1	984.8	963.3	–	932.0	–	911.9
250	1045.9	1016.6	993.1	972.0	952.7	938.9	926.6	915.6
260	1046.4	1018.9	998.6	977.0	958.3	943.7	931.6	919.2
270	1045.4	1019.9	1000.3	980.0	961.2	946.9	934.4	920.5
280	1043.6	1018.9	1000.6	980.8	962.7	948.4	935.2	921.1
290	1041.0	1017.1	999.3	980.0	962.0	947.7	934.5	919.7
298	1038.6	1015.0	997.4	978.3	960.4	946.3	932.6	917.1
310	–	1010.7	993.4	974.6	956.4	941.9	927.7	911.2
320	1029.8	1006.6	989.2	970.2	952.2	937.0	922.2	904.4

TABLE S6: Density ρ (in $\mathrm{kg\,m^{-3}}$) at the corresponding temperature and pressure.

are enough to neglect finite size effects. In order to locate the maximum density, we run several MD simulations at constant pressure (NPT) along an isobar (see Table S6). Next, for each isobar, we identify the temperature at which the density reaches a maximum, as indicated by the red triangles in Fig. 4 of the main text: when decreasing the pressure the temperature of maximum density increases up to a pressure of about -100 MPa where the temperature starts decreasing again.

[1] Pallares, G. *et al.* Anomalies in bulk supercooled water at negative pressure. *Proc. Natl. Acad. Sci. U.S.A.* **111**, 7936–7941 (2014).

[2] Zheng, Q., Durben, D. J., Wolf, G. H. & Angell, C. A. Liquids at Large Negative Pressures: water at the Homogeneous Nucleation Limit. *Science* **254**, 829–832 (1991).

[3] Alvarenga, A. D., Grimsditch, M. & Bodnar, R. J. Elastic properties of water under negative pressures. *J. Chem. Phys.* **98**, 8392–8396 (1993).

[4] Shmulovich, K. I., Mercury, L., Thiéry, R., Ramboz, C. & El Mekki, M. Experimental superheating of water and aqueous solutions. *Geochim. Cosmochim. Acta* **73**, 2457–2470 (2009).

[5] El Mekki Azouzi, M., Ramboz, C., Lenain, J.-F. & Caupin, F. A coherent picture of water at extreme negative pressure. *Nat. Phys.* **9**, 38–41 (2013).

[6] El Mekki Azouzi, M., Tripathi, C. P., Pallares, G., Gardien, V. & Caupin, F. Brillouin spectroscopy of fluid inclusions as a paleothermometer for subsurface rocks. *in preparation* (2014).

[7] Abascal, J. L. F. & Vega, C. A general purpose model for the condensed phases of water: TIP4P/2005. *J. Chem. Phys.* **123**, 234505 (2005).

[8] Aragones, J. L. & Vega, C. Plastic crystal phases of simple water models. *J. Chem. Phys.* **130**, 244504 (2009).

[9] Conde, M. M., Vega, C., Tribello, G. A. & Slater, B. The phase diagram of water at negative pressures: Virtual ices. *J. Chem. Phys.* **131**, 034510 (2009).

[10] Aragones, J. Phase Diagram of Water under an Applied Electric Field. *Phys. Rev. Lett.* **107** (2011).

[11] Vega, C., Abascal, J. L. F. & Nezbeda, I. Vapor-liquid equilibria from the triple point up to the critical point for the new generation of TIP4P-like models: TIP4P/Ew, TIP4P/2005, and TIP4P/ice. *J. Chem. Phys.* **125**, 034503 (2006).

[12] Vega, C., Abascal, J. L. F., Conde, M. M. & Aragones, J. L. What ice can teach us about water interactions: a critical comparison of the performance of different water models. *Faraday Discuss.* **141**, 251–276 (2008).

[13] Aragones, J. L., MacDowell, L. G. & Vega, C. Dielectric constant of ices and water: A lesson about water interactions. *J. Phys. Chem. A* **115**, 5745 (2011).

[14] Vega, C. & Abascal, J. L. F. Simulating water with rigid non-polarizable models: a general perspective. *Phys. Chem. Chem. Phys.* **13**, 19663–19688 (2011).

[15] Hess, B., Kutzner, C., van der Spoel, D. & Lindahl, E. GROMACS 4: Algorithms for Highly Efficient, Load-Balanced, and Scalable Molecular Simulation. *J. Chem. Theory Comput.* **4**, 435–447 (2008).

[16] Van Der Spoel, D. *et al.* GROMACS: Fast, flexible, and free. *J. Comput. Chem.* **26**, 1701–1718 (2005).

[17] Essmann, U. *et al.* A smooth particle mesh Ewald method. *J. Chem. Phys.* **103**, 8577–8593 (1995).

[18] Ryckaert, J.-P., Ciccotti, G. & Berendsen, H. J. C. Numerical integration of the cartesian equations of motion of a system with constraints: molecular dynamics of n-alkanes. *Journal of Computational Physics* **23**, 327–341 (1977).

[19] Nosé, S. A unified formulation of the constant temperature molecular dynamics methods. *J. Chem. Phys.* **81**, 511–519 (1984).

[20] Hoover, W. G. Canonical dynamics: Equilibrium phase-space distributions. *Phys. Rev. A* **31**, 1695–1697 (1985).

[21] Parrinello, M. & Rahman, A. Polymorphic transitions in single crystals: A new molecular dynamics method. *J. Appl. Phys.*

52, 7182–7190 (1981).

[22] The International Association for the Properties of Water and Steam. Revised release on the IAPWS formulation 1995 for the thermodynamic properties of ordinary water substance for general and scientific use (2014). http://www.iapws.org/relguide/IAPWS95-2014.pdf, Date of access: 15/01/2015.

[23] Davis, L. A. Compression of Mercury at High Pressure. *J. Chem. Phys.* **46**, 2650 (1967).

[24] Dávila, M. J. & Martin Trusler, J. Thermodynamic properties of mixtures of n-methyl-2-pyrrolidinone and methanol at temperatures between 298.15 K and 343.15 K and pressures up to 60 MPa. *J. Chem. Thermodyn.* **41**, 35–45 (2009).

[25] Thompson, A. B., Raz, U. & Girsperger, S. Thermal expansion, compressibility and volumetric changes of quartz obtained by single crystal dilatometry to 700 C and 3.5 kilobar (0.35 GPa). *Schweiz. Mineral. Petrogr. Mitteilungen* **82**, 561–574 (2002).

[26] Ohno, I., Harada, K. & Yoshitomi, C. Temperature variation of elastic constants of quartz across the α - β transition. *Phys. Chem. Miner.* **33**, 1–9 (2006).

[27] Tarumi, R., Nakamura, K., Ogi, H. & Hirao, M. Complete set of elastic and piezoelectric coefficients of α-quartz at low temperatures. *J. Appl. Phys.* **102**, 113508 (2007).

[28] Landau, L. D. & Lifshitz, E. M. *Theory of Elasticity* (Elsevier, 1986).

[29] Holten, V. & Anisimov, M. A. Entropy-driven liquid-liquid separation in supercooled water. *Sci. Rep.* **2**, 713 (2012).

[30] Holten, V., Anisimov, M. A. & Sengers, J. V. Towards a supercooled water guideline. Technical Report, International Association for the Properties of Water and Steam (2012).